This document is the accepted manuscript version of the following article:
Aellen, M., Rossinelli, A. A., Keitel, R. C., Brechbühler, R., Antolinez, F. V., Rodrigo, S. G., … Norris, D. J. (2022). Role of gain in Fabry-Pérot surface plasmon polariton lasers. ACS Photonics, 9(2), 630-640. https://doi.org/10.1021/acsphotonics.1c01627

The Role of Gain in Fabry–Pérot Surface Plasmon Polariton Lasers

Marianne Aellen[†], *Aurelio A. Rossinelli*[†], *Robert C. Keitel*[†], *Raphael Brechbühler*[†], *Felipe V. Antolinez*[†], *Sergio G. Rodrigo*[‡,§], *Jian Cui*[†,||], *and David J. Norris*[†,*]

[†]Optical Materials Engineering Laboratory, Department of Mechanical and Process Engineering, ETH Zurich, 8092 Zurich, Switzerland

[‡]Departamento de Física Aplicada, Facultad de Ciencias, Universidad de Zaragoza, 50009 Zaragoza, Spain

[§]Instituto de Nanociencia y Materiales de Aragón (INMA), CSIC-Universidad de Zaragoza, 50009 Zaragoza, Spain

[||]Helmholtz Pioneer Campus, Helmholtz Zentrum München, 85764 Neuherberg, Germany

ABSTRACT. Plasmonic lasers generate strongly confined electromagnetic fields over a narrow range of wavelengths. This is potentially useful for enhancing nonlinear effects, sensing chemical species, and providing on-chip sources of plasmons. By placing a semiconductor gain layer near a metallic interface with a gap layer in between, plasmonic lasers have been demonstrated. However, the role of gain in this common design has been understudied, leading to suboptimal choices. Here, we examine planar metallic lasers and explore the effect of gain on the lasing behavior. We print semiconductor nanoplatelets as a gain layer of controllable thickness onto alumina-coated silver films with integrated planar Fabry–Pérot cavities. Lasing behavior is then monitored with spectrally and polarization-resolved far-field imaging. The results are compared with a theoretical waveguide model and a rate-equation model, which consider both plasmonic and photonic modes and explicitly include losses and gain. We find that the nature of the lasing mode is dictated by the gain-layer thickness, and, contrary to conventional wisdom, a gap layer with high refractive index can be advantageous for plasmonic lasing in planar Fabry–Pérot cavities. Our rate-equation model also reveals a regime where plasmonic and photonic modes compete in an unintuitive way, potentially useful for facile, active mode switching. These results can guide future design of metallic lasers and could lead to on-chip lasers with controlled photonic and plasmonic output.

KEYWORDS. plasmonic laser, spaser, metallic laser, nanoplatelets, threshold gain, mode competition

Surface plasmon polaritons (shortened here to surface plasmons) are electromagnetic waves coupled to electronic oscillations at a metal–dielectric interface.[1,2] They allow tighter mode confinement than photons, and thus enable large near-field intensities that can be strongly localized. This enables optical sensing of molecules,[3] enhances nonlinear effects,[4] and reduces the size of integrated circuits for electromagnetic waves.[5-11] However, one disadvantage of plasmonic devices is that the metal introduces significant loss,[12] resulting in short propagation lengths and broad resonance linewidths, which severely limits device applications. Consequently, structures that amplify surface plasmons through stimulated emission have been developed.[13] This has led to plasmonic lasers (or "spasers"),[14,15] which combine gain with a plasmonic resonator. While the goal of initial devices was to produce nanoscale sources of photons, different designs have been pursued, including those that aim at generating surface plasmons. With narrow linewidths and intense fields, these latter devices can be useful for sensing, optical probing, and near-field spectroscopy.[16]

The first demonstration of lasing in a surface-plasmon mode utilized a semiconductor nanowire (for gain) that was placed on top of a plasmonic metal with a dielectric gap layer in between.[17] The nanowire ends serve as reflectors, creating a linear Fabry–Pérot cavity for surface plasmons. Similar designs, but with different materials, have extended operational wavelengths from the ultraviolet to the near-infrared and have further improved performance, including decreased thresholds and room-temperature operation.[18-25] However, because these devices were fabricated through random placement of semiconductor nanostructures (wires, flakes, etc.) on a substrate, methods have been sought to create resonators via top-down techniques for easier integration. Metal-clad layers of epitaxially grown semiconductors can be employed, which also allow for electrical pumping.[26-28] Alternatively, a planar Fabry–Pérot cavity can be created on a flat metal interface (see schematic next to the abstract). Surface plasmons then bounce back and forth between reflectors incorporated into the metal surface.[29,30] A gain material compensates metal and cavity losses allowing lasing of the surface-plasmon mode. Although these planar Fabry–Pérot lasers tend to be larger in size, they offer tremendous flexibility in terms of adding gain materials by simple coating or printing techniques and for controlling the plasmonic output through lithographic cavity design and integration.

In any plasmonic laser, an important issue is the character of the lasing modes. Depending on the cavity design, both plasmonic and photonic modes can exist. In the early nanowire plasmonic lasers,[17,20] the lasing mode was determined by measuring photons scattered from the cavity ends. As plasmonic modes are transverse-magnetic (TM) and photonic modes are transverse-electric (TE), plasmonic modes scatter into photons polarized along the nanowire axis. In many later plasmonic lasers, such polarization measurements were not reported. Rather, alternative evidence was provided. For example, the authors of Ref. 29 on planar Fabry–Pérot cavities with colloidal quantum dots as the gain medium found that polarization experiments were ambiguous. Thus, they instead compared the measured free spectral range of the cavity to calculations. In addition, plasmonic lasing was thought to be consistent with the cavity design, which utilized thin (~100 nm) gain layers and reflectors that were lossy for photons. However, later experiments showed that these devices were actually lasing in the photonic mode. Thus, planar Fabry–Pérot plasmonic lasers[29,30] should be revisited to determine the conditions under which they can generate lasing of surface plasmons.

A deeper understanding of these devices requires a thorough experimental and theoretical investigation of their design, including the gain, the gain-layer thickness, and the dielectric gap layer. These design choices greatly influence the interaction of the mode with the gain. For example, it is often argued that a low-refractive-index gap layer assists plasmonic lasing because the electromagnetic energy is concentrated in the low-refractive-index dielectric, thus reducing metallic losses.[17,19,22,24,31] This is correct for passive waveguide structures for which no loss compensation is required and the propagation losses must simply be minimized.[5] However, the choice of a low-index gap layer also affects the interaction of the mode with the waveguiding structure on top, which, in the case of a plasmonic laser, is the gain medium. Not including the effect of gain for devices where loss compensation is a requirement potentially results in sub-optimal laser designs. Moreover, the thickness of the semiconductor layer has not been explored with respect to the gain it provides to a given mode. This thickness not only dictates the confinement but, more importantly, the nature of the lasing mode (i.e., whether a plasmonic or photonic mode is coherently amplified). Indeed, plasmonic lasers are often distinguished from their photonic counterparts by comparing a plasmonic design with an equivalent structure in which the metal has been replaced by a dielectric material.[17,19,32] However, this approach is insufficient for many plasmonic devices whose dimensions allow both plasmonic and photonic modes, especially in systems where the mirror reflectivities of both modes are comparable. The coexistence and competition of these modes in metallic lasers must be systematically investigated, including the role of both losses and gain, for a full understanding of these devices.

Here, we provide such an investigation by treating the common semiconductor–insulator–metal laser structure with a gain layer of precisely controlled thickness combined with metallic mirrors that are highly reflective for strongly and weakly guided modes. We select films of colloidal semiconductor nanoplatelets (NPLs) and alumina for the gain and gap layers, respectively. The NPLs are then optically pumped to observe lasing. By combining spectrally and polarization-resolved far-field measurements with a theoretical waveguide model that explicitly includes losses and gain, we show how the gain-layer thickness largely determines whether a device lases in the plasmonic or photonic mode. Next, we theoretically revisit the design choice for the gap layer and find that whether a high- or low-refractive-index gap is advantageous for plasmonic lasing strongly depends on whether gain is included in the waveguide model or not. Finally, by looking at the pump-power-dependent output intensities of our laser devices, our measurements and calculations reveal a previously unstudied regime where plasmonic and photonic modes coexist and compete for gain in an unintuitive manner. This behavior, elucidated by a rate-equation model that explicitly accounts for both types of modes, leads to the possibility of switching between plasmonic and photonic lasing within the same device. More generally, our study clarifies the interplay of loss and gain in multilayer metallic Fabry–Pérot lasers and provides broader insights for the understanding of these devices.

RESULTS AND DISCUSSION

Device Fabrication. Our devices were fabricated through a three-step process with fine control over the thickness and quality of the constituent materials. Our cavities consist of two 500-nm-tall silver (Ag) reflectors on a smooth Ag substrate, forming a stable, 10-μm-long Fabry–Pérot resonator (Figure 1a). The reflector shape is parabolic with a radius of curvature of 20 μm. The low roughness of the Ag, achieved by template stripping,[33,34] minimizes propagation losses while the reflectors serve as efficient mirrors for both plasmonic and photonic modes.[35,36] Using atomic layer deposition, the cavities were then coated with 10 nm of alumina, which serves both as the gap layer and prevents Ag degradation. Finally, a 2-μm-wide stripe of colloidal CdSe/$Cd_xZn_{1-x}S$ core/shell NPLs[37] was placed between the reflectors using electrohydrodynamic nanoprinting.[38] By tuning the printing parameters, the thickness of the NPL stripe could be precisely controlled.

Coexisting Waveguide Modes. A critical complication of planar, multilayer devices is that they can support both plasmonic and photonic propagating modes, any of which can potentially lase. Using a theoretical multilayer-waveguide model (see Methods), which consists of a semi-infinite Ag layer, a 10-nm alumina layer, a NPL gain layer of variable thickness d_{gain}, and a semi-infinite air layer, we could identify the TM and TE modes at a free-space wavelength $\lambda_0 = 635$ nm (Figure 1b). Below a gain-layer thickness of 150 nm, only the fundamental TM and TE modes exist. The TM mode is plasmonic, localized at the Ag–dielectric interface, and exists even at vanishingly thin gain layers. The TE mode is photonic and ceases to exist below a gain-layer thickness of ~70 nm (Figure 1c). This "cutoff" is a key characteristic of the photonic mode.

Spectrally and polarization-resolved far-field measurements reveal the existence of plasmonic and photonic modes in our devices. Within our Fabry–Pérot cavities, propagating modes form longitudinal standing waves. These cavity modes are revealed when we optically excite the NPL stripe with a light-emitting diode (LED). Figure 1d plots the leakage spectrum for light scattered at the inner reflector edge for a device at 4 K. The cavity resonances appear within the spontaneous-emission bandwidth of the colloidal NPLs. Whether a resonance originates from a plasmonic or photonic mode can be distinguished using a linear polarizer. Plasmonic (photonic) modes scatter at the reflector into photons with an electric-field component parallel (perpendicular) to the cavity long axis (z-direction, see schematic in Figure 1a). These photons are collected in the far-field by our microscope objective. Note that the photonic resonances are more intense than the plasmonic resonances. This is a consequence of higher metal loss and a lower collection efficiency for far-field photons scattered from plasmonic modes than for photons scattered from photonic modes.

The free spectral range (FSR) further confirms that polarization can be used to distinguish between plasmonic and photonic modes, even within the same device. The measured FSR of TM- and TE-polarized cavity modes display two distinct regimes that exhibit a trend closely matching calculated values (see Methods; Figure 1e). Note that the reflectors are fairly tall and thus provide good reflectivity also for weakly-guided photonic modes at gain-layer thicknesses close to their cutoff. Our calculation slightly overestimates the FSR for the photonic mode, perhaps because it does not capture lateral confinement effects. We hypothesize that, close to its cutoff, the photonic mode strongly extends toward the edges of our NPL stripes in the transverse in-plane direction. This would introduce a stronger waveguide dispersion that results in a higher group index and, therefore, a decreased FSR compared to the calculated values. Despite this slight discrepancy, our waveguide model captures all salient features of the plasmonic and photonic modes as resolved by polarization in our far-field measurements.

Lasing from Photonic and Plasmonic Modes. To characterize lasing, we optically pumped cavities at 4 K with a defocused pulsed laser beam (Figure 2a,b; lasing at higher temperatures is discussed in Supporting Information, Section S1). As above, we collect the leakage spectrum of light scattered at the inner edge of a cavity reflector. At low excitation fluences, broad-band spontaneous emission dominates the cavity spectrum. With increasing pump fluence, distinct lasing peaks appear. As previously shown for the cavity spectra under LED excitation, polarization can be used to resolve which lasing peaks represent photonic and plasmonic modes. In a device with a thin gain layer (d_{NPL} = 56 nm, Figure 2c), the lasing emission is TM-polarized—indicative of plasmonic lasing. For a thicker gain layer (d_{NPL} = 74 nm, Figure 2d), photonic (TE-polarized) lasing is observed. Even though the spectra of these comparable devices look similar, the underlying nature of the lasing mode is different and can be determined through polarization-resolved measurements.

We assessed the influence of the gain-layer thickness on the lasing mode by probing twelve devices of differing NPL-stripe thicknesses. All devices were fabricated on the same substrate to eliminate potential variations in quality or thickness of the Ag and alumina. Their lasing modes were assigned based on their out-scattered polarization. For all devices, the intensity of the lasing peak under one polarization direction was at least one order of magnitude greater than in the orthogonal direction. Hence, each d_{NPL} could be associated with lasing in the plasmonic or the photonic mode, revealing two regimes. For $41\ \mathrm{nm} \leq d_{\mathrm{NPL}} \leq 66\ \mathrm{nm}$, plasmonic lasing was observed, while for $74\ \mathrm{nm} \leq d_{\mathrm{NPL}} \leq 85\ \mathrm{nm}$, photonic lasing was found (Figure 2e). For the device with $d_{\mathrm{NPL}} = 24\ \mathrm{nm}$, lasing could not be achieved, even at the highest pump fluence. While the cavity spectra under LED excitation showed the coexistence of plasmonic and photonic modes for gain layers thicker than the photonic-mode cutoff (Figure 1d), only photonic lasing was observed in these devices.

Modal-Gain Calculations Predict Gain-Layer Requirements. The dependence on gain-layer thickness can be understood using a modified version of our multilayer-waveguide model. Instead of treating the gain layer as transparent, as is commonly done when optimizing for the modal propagation length,[5] we included material gain. The material gain describes the gain per unit length that a plane wave would experience in a uniform infinitely extended medium under a specific set of conditions (excitation density, temperature, etc.). To describe the gain experienced by a confined mode in our multilayer-waveguide structure, we then need to determine the modal gain, G_{mod}, which is calculated from the imaginary part of the propagation constant, k_z'', of the respective mode, through $G_{\mathrm{mod}} = -2k_z''$ (Ref. 39). The modal gain incorporates both ohmic losses from the Ag and material gain from the gain medium. These are included as positive (loss) or negative (gain) values in the imaginary part of the relative permittivity of the Ag and the gain layers, respectively (see Methods). The alumina and air are assumed to be lossless with purely real permittivity values.

To achieve lasing, all cavity losses must be compensated by gain. The Ag losses (contained in G_{mod}) and reflection losses represent the main loss channels (see Supporting Information, Section S2), resulting in the following condition for lasing:

$$G_{\mathrm{mod}} \geq -\frac{\ln(R)}{L_{\mathrm{cav}}}, \tag{1}$$

where R is the mirror reflectivity and L_{cav} the cavity length (see Supporting Information, Section S3 for derivation). The reflectivity of our Ag reflectors is estimated to be ~90% for both plasmonic and photonic modes (see Supporting Information, Section S4).[35,36] Hence, lasing in our 10-μm-long cavities can only be obtained for a modal gain equal to or greater than our reflection losses of 105 cm^{-1}.

We can calculate the modal gain for a range of material gains, G_{mat}, and gain-layer thicknesses, d_{gain}, to understand the requirements for lasing in plasmonic and photonic modes. For a transparent gain layer ($G_{\mathrm{mat}} = 0\ \mathrm{cm}^{-1}$, dotted lines in Figure 3), the modal gain is negative—indicative of dissipative mode propagation due to Ag losses. The plasmonic mode suffers from higher losses than the photonic mode (blue and red dotted lines, respectively, in Figure 3) for any fixed gain-layer thickness due to the strong localization of the plasmonic mode inside the Ag (Figure 1b). With a material gain of $G_{\mathrm{mat}} = 1500\ \mathrm{cm}^{-1}$ (dashed lines in Figure 3), the photonic mode compensates propagation and reflection losses when the gain-layer thickness is slightly above the photonic-mode cutoff ($d_{\mathrm{gain}} > 71$ nm). This is depicted in Figure 3 when the red dashed line rises above the horizontal grey line, which represents reflection losses in our cavity. At this thickness, the plasmonic mode is still dominated by losses (blue, dashed line in Figure 3). This agrees with experiments, where photonic lasing is observed for $74\ \mathrm{nm} \le d_{\mathrm{NPL}} \le 85$ nm. For $G_{\mathrm{mat}} = 2500\ \mathrm{cm}^{-1}$ (solid lines in Figure 3), the modal gain of the plasmonic mode fulfills the lasing condition for $d_{\mathrm{gain}} > 41$ nm. Our observation of plasmonic lasing for $41\ \mathrm{nm} \le d_{\mathrm{NPL}} \le 66$ nm is completely consistent with these calculations. We note that CdSe NPLs can provide such high gain values.[40,41] Therefore, our multilayer-waveguide model, which includes gain, accurately describes the experimental dependence of the lasing mode on the NPL-stripe thickness, assuming that a range of material-gain values can be attained upon excitation of the NPL stripe.

Figure 3 also reveals another interesting effect. Even though the photonic mode experiences significantly lower Ag losses, the plasmonic mode displays a larger modal gain than the photonic mode for $G_{\mathrm{mat}} = 2500\ \mathrm{cm}^{-1}$ and $69\ \mathrm{nm} < d_{\mathrm{gain}} < 84$ nm (grey shaded area in Figure 3). We discuss this counter-intuitive result in detail further below. Briefly, the modal gain depends not only on the Ag losses and the material gain but also on the mode confinement within the gain layer. We can express the modal gain in terms of the confinement factor, Γ, through[39]

$$G_{\mathrm{mod}} = \Gamma \cdot G_{\mathrm{mat}} - \frac{1}{L_{\mathrm{prop}}}, \tag{2}$$

where L_{prop} is the propagation length of the mode for a transparent gain layer ($G_{\mathrm{mat}} = 0\ \mathrm{cm}^{-1}$). We avoid the complication of finding an analytical expression for the confinement factor[39] by computationally sweeping over the material gain and extracting the confinement factor and propagation length from a linear fit to the modal gain (see Supporting Information, Section S5). In follow-up work we will discuss the confinement factor and its relevance for the calculation of loss and gain in more detail. While the plasmonic mode suffers larger losses than the photonic mode (equivalent to having a shorter propagation length; Supporting Information, Figure S4b), its confinement factor is notably larger (Supporting Information, Figure S4c). Therefore, the plasmonic mode achieves a larger modal gain than the photonic mode when the following condition is met:

$$G_{\mathrm{mat}} > \frac{\Delta\alpha_{\mathrm{prop}}}{\Delta\Gamma}\ , \tag{3}$$

with $\Delta\alpha_{\mathrm{prop}} = (1/L_{\mathrm{prop,TM}} - 1/L_{\mathrm{prop,TE}})$ and $\Delta\Gamma = \Gamma_{\mathrm{TM}} - \Gamma_{\mathrm{TE}}$. According to this mode condition (eq 3), the mode with larger G_{mod} is determined not only by d_{gain} but also by the exact value of G_{mat}. This effect remains unnoticed if gain is not explicitly included in the mode calculations.

The relevant metric for lasing is the threshold gain—the minimum material gain required to achieve loss compensation. Using the lasing condition (eq 1) and the modal-gain expression (eq 2), the threshold gain, G_{th}, is defined as:

$$G_{\mathrm{th}} = \frac{1}{\Gamma}\left(\frac{1}{L_{\mathrm{prop}}} - \frac{\ln(R)}{L_{\mathrm{cav}}}\right)\ , \tag{4}$$

The smaller the threshold gain, the lower the required excitation density in the gain medium to achieve lasing. This is especially desirable for designs where heating poses an upper limit to the device performance (a common complication in nanolasers[42-44]).

The threshold-gain expression (eq 4) can explain the lack of lasing in the device with the thinnest NPL stripe. With $d_{\mathrm{gain}} = 24$ nm, we calculate $G_{\mathrm{th}} > 4000\ \mathrm{cm}^{-1}$ (Supporting Information, Figure S4d). Such a high G_{mat} can only be achieved under extremely high pump fluences.[40,41] Unfortunately, the emission intensity of our NPL stripes decreased irreversibly when the pump fluence was too high, presumably due to detrimental heating effects. Therefore, the threshold gain (and thus lasing) could not be attained. We note that eq 4 applies to any mode in any Fabry–Pérot-cavity laser, including more complex two-dimensional waveguide systems. This expression not only predicts whether lasing can be achieved in a given mode but allows selection of the appropriate gain material by including material properties that are independent of the design.

Reconsidering the Gap-Layer Refractive Index. Our multilayer-waveguide model can also be used to analyze the second key component of planar plasmonic lasers—the dielectric gap layer. Because the effect of gain has not always been fully treated in the literature, incorrect conclusions about the gap layer can result. In particular, early plasmonic lasers exploited low-index dielectric layers to confine the electric field inside the gap to reduce losses from the metal.[17,19,20,22-24,32] However, the reasoning for this choice was based on the calculation of surface-plasmon propagation lengths in passive (i.e., $G_{\mathrm{mat}} = 0\ \mathrm{cm}^{-1}$) waveguide structures.[5] Thus, the choice of a low-index layer should be revisited to assess whether it is indeed advantageous for plasmonic lasers.

We theoretically compared the plasmonic modes of the same waveguide structure as above, but with the gap layer replaced by either a low-index dielectric, e.g., magnesium fluoride ($n_{\mathrm{gap}} = 1.42$), or a high-index dielectric, e.g., titanium dioxide ($n_{\mathrm{gap}} = 2.13$). Assuming a transparent gain layer ($G_{\mathrm{mat}} = 0\ \mathrm{cm}^{-1}$), the low-index-gap (LIG) structure achieves larger modal gains than the high-index-gap (HIG) structure for any fixed gain-layer thickness (dashed lines Figure 4a) due to reduced mode localization inside the Ag layer. This agrees with previous considerations.[5] However, when high material gain is included ($G_{\mathrm{mat}} = 2500\ \mathrm{cm}^{-1}$), the opposite is observed (solid lines Figure 4a). For thicker gain layers, the HIG structure experiences higher modal gain than the LIG structure and thus can potentially cope with higher reflection losses. This contradicts generally accepted design rules for plasmonic lasers and requires a closer analysis of how the material gain dictates which device configuration experiences a higher modal gain, and ultimately, the material gain needed to achieve lasing.

We evaluated the material-gain values that allow a HIG structure to experience a larger modal gain than the LIG structure. Therefore, we applied the mode condition in eq 3, but instead of comparing the plasmonic and photonic modes of the same structure, we compared the plasmonic modes of the HIG and LIG structures. For low material-gain values ($G_{\mathrm{mat}} < 2000\ \mathrm{cm}^{-1}$) or thin gain-layers, the LIG structure experiences a larger modal gain (light-green area in Figure 4b) than the HIG structure (dark-green area in Figure 4b). However, the relative difference in modal gain only tells us which structure experiences higher net gain, but not whether its mode can actually lase.

Using the threshold gain (eq 4), we can identify the material gain for which loss compensation (and thus lasing) in the plasmonic mode is possible. Assuming a cavity with perfect mirrors (see blue solid and dashed lines labeled $R = 1.0$ in Figure 4b), the crossing point of the threshold gain for the two structures (HIG and LIG) is at $d_{\text{gain}} \approx 43$ nm. For devices with thinner (thicker) gain layers, a high-index (low-index) gap layer is preferred, as the threshold gain is lower for this structure.

Upon introducing reflection losses ($R < 1.0$), the threshold-gain crossing point moves along the mode-condition border (i.e., the border between the light- and dark-green areas in Figure 4b) toward thicker gain layers, extending the range of gain-layer thicknesses for which the HIG structure is preferred. Additionally, the difference in threshold gain between the HIG and LIG structures becomes significantly larger the thinner the gain layer (left of the crossing point). For example, for $R = 0.5$ in a 10-μm long cavity and $d_{\text{gain}} = 40$ nm, the LIG-structure threshold gain is 18.4% larger than the HIG-structure threshold gain, an amount that can be decisive in achieving lasing. Therefore, a LIG structure is only advantageous for plasmonic lasers with a high mirror reflectivity and a thick gain layer. However, for thick gain layers, the photonic mode could become the prevailing lasing mode due to lower Ag losses (see cutoff thickness for the photonic mode in Figure 4b). For plasmonic lasers with gain-layer thicknesses well below the photonic-mode cutoff thickness, the HIG structure exhibits a lower threshold gain and thus requires lower excitation densities to achieve lasing.

The effect of gain on the overall lasing conditions has mostly been overlooked when designing plasmonic lasers. Instead, the focus was placed primarily on reducing metal propagation losses. In cavities that employ a semiconductor gain layer with a higher refractive index than exhibited by NPL films (e.g., $n_{\text{gain}} > 2$ instead of NPL films with $n_{\text{NPL}} = 1.89$, see Supporting Information, Section S6), the difference in threshold gain between the HIG and LIG structures is even greater (Supporting Information, Figure S5a,b), showcasing the advantage of high-index gap layers for other material systems. Similar conclusions were found in two-dimensional waveguide calculations.[45] In principle, removing the gap layer altogether would further reduce the threshold gain (Supporting Information, Figure S5c). However, this renders the Ag prone to degradation and increases quenching rates especially when single-crystal semiconductors are employed as gain material.[46] More generally, the role of the gap layer is only adequately judged if gain is explicitly treated in the mode calculations, a conclusion that also applies to other plasmonic-laser designs.

Pump-Power Dependence on Lasing Dynamics. So far, we have evaluated design criteria based on a static material gain. However, experimentally, the material gain will be a function of the pump intensity and thus will be strongly time dependent under pulsed excitation. We first investigate the output intensity as a function of pump fluence (light–light curve) and then model the findings with rate equations that disclose mode-dependent lasing dynamics beyond findings from a static material gain.

We experimentally measured the light–light curves for two devices (one displaying plasmonic and the other photonic lasing) by extracting the integrated intensity of lasing spectra at various pump fluences (filled circles in Figure 5a,b). The light–light curves look quite different. While the output of the device with $d_{\mathrm{NPL}} = 56$ nm remains nearly linear with input even when lasing begins [recognizable by the increasing predominance of a narrow peak in the output emission (Figure 2a), which causes the overall linewidth of the emission spectrum to drop (empty circles in Figure 5a)], the device with $d_{\mathrm{NPL}} = 74$ nm shows a marked inflection at the corresponding lasing threshold. To elucidate this behavior, we set up a rate-equation model (see Methods) with which we calculated the light–light curves (dotted lines in Figure 5a,b). Without any fitting (apart from a normalization to account for the unknown collection efficiency), our model can reproduce the light–light curves for both experimentally probed devices.

Using our rate-equation model, we can then study the difference in the light–light curves by looking at the excited-carrier population that feeds into the lasing mode above and below threshold. Above threshold, nearly all carriers decay into the lasing mode, while below threshold, only a fraction does (see Supporting Information, Section S7). This fraction is $\beta_i \Phi$, where β_i is the spontaneous-emission factor of the mode i (i = TM or TE) and Φ is the quantum yield of the gain medium. β_i can be calculated from the power dissipated by a position- and orientation-averaged electric point dipole into the respective mode (see Supporting Information, Section S8). We assume Φ is 88%, as measured for our NPLs in hexane dispersion at room temperature.[37] In a waveguide structure with a 10-nm alumina gap layer, $\beta_{\mathrm{TE}} < 10\%$ for $d_{\mathrm{gain}} = 74$ nm, while $\beta_{\mathrm{TM}} > 70\%$ for $d_{\mathrm{gain}} = 56$ nm. The large β_{TM} is indicative of a highly confined, sub-diffraction mode, as observed in numerous nanolasers.[17,47] These values explain why the device with $d_{\mathrm{NPL}} = 74$ nm exhibits a superlinear increase in the output intensity at the threshold. Only ~8% of the carriers feed into the photonic mode below threshold. In contrast, for the device with $d_{\mathrm{NPL}} = 56$ nm, > 60% of the carriers already decay into the plasmonic mode below threshold. Consequently, the output intensity does not rise dramatically upon reaching threshold and the light–light curve remains linear. Therefore, the metallic-cavity lasers studied here, despite only differing in gain-layer thickness, exhibit strikingly different light–light curves due to the different nature of their lasing modes.

Our rate-equation model not only describes these light–light curves, but also the time-dependent lasing dynamics, allowing the mode competition between coexisting waveguide modes to be understood. Returning to the light–light curve for $d_{\mathrm{gain}} = 74$ nm, we can appreciate why photonic lasing is observed in the device even though the modal gain of the plasmonic mode is expected to be larger at $G_{\mathrm{mat}} = 2500\ \mathrm{cm}^{-1}$ (see grey area in Figure 3). Using the model, we can determine the output-photon number of each mode separately. (For simplicity, we use the term “output photon” for both surface plasmons and photons that are lost through imperfect reflection at the cavity mirrors.) We find that the photonic mode exceeds its threshold at a pump fluence of 15 $\mu\mathrm{J/cm}^2$ (diamond 1 in Figure 5c). This is consistent with the photonic laser pulse in the time evolution of the output-photon rate (panel 1 in Figure 5d). Concurrently, the plasmonic output-photon number decreases because the photonic mode quickly depletes the carrier population through stimulated emission. The threshold gain of the photonic mode (eq 4) is reached before the mode condition (eq 3) can be fulfilled for the plasmonic mode. Even though the confinement factor is larger for the plasmonic mode, the decreased losses of the photonic mode allow photonic lasing at lower pump fluences. Hence, in agreement with experiments on devices with $74\ \mathrm{nm} \leq d_{\mathrm{NPL}} \leq 85$ nm, the photonic mode always reaches its lasing threshold before potential plasmonic lasing can be observed. This assumes low reflection losses for both modes, which is typical for metallic-cavity lasers (see Supporting Information, Section S9 for the required difference in reflectivity needed to reach the plasmonic threshold gain first).

Even though the photonic mode is the prevailing lasing mode for a metallic-cavity laser with d_{NPL} = 74 nm, our rate-equation model predicts that plasmonic lasing can be achieved if the material gain is sufficiently high. At a pump fluence of 23 μJ/cm^2, the plasmonic mode also exceeds its lasing threshold, as evident from the appearance of a plasmonic laser pulse in the time evolution of the output-photon rate (panel 2 in Figure 5d). At higher pump fluences, the plasmonic mode begins to outcompete the photonic mode, leading to an inversion of their output-photon numbers. For example, plasmonic lasing dominates at 32 μJ/cm^2 (panel 3 in Figure 5d), effectively giving rise to a switching of the primary lasing mode from photonic to plasmonic within the same device. This behavior originates from the difference in confinement factor (as discussed above). At large pump fluences, the material gain is high, and therefore, the mode condition (eq 3) is met, resulting in strong carrier-population depletion by the plasmonic mode, and thus, a reduced photon population. Although our experimentally probed devices displayed signs of degradation when the pump fluence was increased far beyond the photonic lasing threshold, the predicted switching mechanism would in principle result in a new type of laser device that could be used as a single controllable source of coherent photons or coherent surface plasmons.

CONCLUSIONS

In summary, our study demonstrates the importance of considering gain when designing plasmonic lasers. We fabricated metallic Fabry–Pérot cavity lasers with a precisely controlled thickness of the gain layer consisting of colloidal NPLs. Lasing was observed in plasmonic and photonic modes, depending on the gain-layer thickness. Our multi-layer waveguide model that explicitly treats losses and gain explained these findings. Furthermore, we re-evaluated the choice of the gap-layer between the metal and semiconductor layer in plasmonic laser designs. In contrast to what is commonly accepted, we find that a high-index gap layer is preferred for plasmonic lasers with a gain-layer thickness well below the photonic-mode cutoff thickness. This conclusion was enabled by explicitly considering gain in our multi-layer waveguide model, and minimizing the threshold gain, rather than just the metal losses, as has been done in previous studies. Our theoretical findings further revealed the possibility of a device that switches its dominant lasing mode from photonic to plasmonic upon increasing the pump fluence. Such a device could then serve as an on-chip laser with a switchable output of plasmonic and photonic modes.

METHODS

Fabrication of Laser Cavities. Ag cavities were fabricated by template stripping to achieve a smooth Ag surface.[34] The templates were prepared from 1-mm-thick, 2-inch-diameter, <100> silicon wafers. An electron-beam-lithography step (Vistec Lithography, EBPG 5200+) and a subsequent hydrogen-bromide-based inductively-coupled-plasma reactive-ion etch (Oxford Instruments, Plasmalab System 100) resulted in ~500-nm-deep patterns (for the reflectors) in the template (see Supporting Information, Section S10 for a description of the cavity geometry).

A film of Ag (Kurt J. Lesker, 99.99%) ~700 nm thick was then deposited on the template through thermal evaporation (Kurt J. Lesker, Nano36) at a base pressure of $< 9 \times 10^{-8}$ mbar and at a deposition rate of 25 Å/s while the template was rotated at 60 rpm. A microscope slide was bonded to the Ag film using epoxy (Epoxy Technology, EPO-TEK OG116-31) that was cured under ultraviolet light for ~2 h. The Ag cavities were stripped manually from the template shortly before alumina was deposited at 50 °C via 100 atomic-layer-deposition cycles (Picosun, Sunale R-150). The templates were reused multiple times.

The gain layer involved $CdSe/Cd_xZn_{1-x}S$ core/shell NPLs with 4-monolayer-thick CdSe cores and 2-nm-thick shells.[37] The ink for the electrohydrodynamic nanoprinting was prepared by transferring the NPLs from hexane to tetradecane through selective evaporation while adjusting the concentration to an optical density of 5.0 (measured at the lowest-energy exciton peak using a quartz cuvette with a 10-mm path length). A description of the nanoprinting setup can be found elsewhere.[48] Printing was performed by applying 250 V direct current between the metal-coated nozzle (+) and the indium-tin-oxide-coated glass sample holder (ground). The 10-μm-long NPL stripes were generated by moving the sample stage in a serpentine-like fashion to print nine parallel lines at a pitch of 250 nm. Different stripe thicknesses were achieved by varying the number of overprints. To determine the required stage velocity and number of overprints to produce a given stripe thickness, a parameter sweep was performed before printing into cavities using the same ink-loaded nozzle. Stripes were printed on a flat Ag–alumina substrate and examined in reflection dark-field mode on an optical microscope [Nikon Eclipse LV100, 50× objective (Nikon CFI LU Plan Fluor BD) with a numerical aperture of 0.8]. The stripe thickness was estimated by comparing the stripe color to a reference image of stripes of known thicknesses. After all optical measurements were performed, the stripe thickness of each device was measured using atomic force microscopy (Bruker, Dimension FastScan). See Supporting Information, Section S10 for a more detailed description of the fabrication methods.

Optical Characterization. All optical measurements were performed in a closed-cycle helium cryostat (Montana Instruments, Cryostation 2 with LWD option) under vacuum and cooled to 4 K. To obtain cavity spectra within the spontaneous-emission bandwidth of the NPLs, the cavities were illuminated by light from a 385-nm LED (Thorlabs, M385LP1). Lasing experiments were performed with 405-nm laser pulses (~340 fs pulse duration, 1 kHz repetition rate) emerging from a collinear optical parametric amplifier (Spectra-Physics, Spirit-OPA) pumped by a 1040-nm laser (Spectra-Physics, Spirit-1040-8). A defocused laser spot of ~30 μm diameter was generated by employing a defocusing lens before the beam was directed through a 60× extra-long-working-distance objective (Nikon, CFI S Plan Fluor ELWD with a numerical aperture of 0.7) to the sample.

The same objective was used to collect emission from the sample. The emission was separated from the excitation through a 405-nm dichroic longpass filter (AHF analysentechnik, F48-403) and further filtered by a 450-nm longpass filter (Thorlabs, FEL0450). Then, the image was relayed into an imaging spectrometer (Andor, Shamrock 303i) with an entrance slit set to 50 μm. The sample was placed such that the inner edge of a cavity reflector was imaged on the vertical entrance slit. The spectrometer dispersed the image horizontally using a 300 lines/mm grating (500-nm blaze) and imaged with an air-cooled electron-multiplying charged-coupled-device camera (Andor, iXon 888 Ultra). For polarization-resolved spectra, a linear polarizer (Thorlabs, LPVISB100-MP2) was placed in an image plane after the 450-nm longpass filter. A detailed description of the optical characterization can be found in the Supporting Information, Section S11.

Multilayer-Waveguide Model. The multilayer-waveguide model was implemented following a theoretical model described in Ref. 49 (see Supporting Information, Section S12 for details). We solved the eigenvalue equation for TM and TE polarized waves by a minimization algorithm. From the resulting propagation constant, k_z, we can derive the effective mode index, n_{eff}, the modal gain, G_{mod}, and the electric- and magnetic-field profiles. As input into the model, the free-space wavelength was set to $\lambda_0 = 635$ nm (1.95 eV) for all calculations except for the FSR calculations, where λ_0 was varied over a range of 500–700 nm (1.48–1.77 eV). The relative permittivity of each constituent material was obtained from ellipsometry (see Supporting Information, Section S13).

Free-Spectral-Range Calculation. The FSR was calculated with[50]

$$E_{\mathrm{FSR}} = \frac{hc}{2 \cdot L_{\mathrm{cav}} \cdot n_{\mathrm{g}}}, \tag{5}$$

where h is Planck's constant, c the speed of light, and n_g the group index. The group index was calculated from the effective mode index and its dispersion (see Supporting Information, Section S14) using

$$n_{\mathrm{g}} = n_{\mathrm{eff}} - \lambda \frac{\partial n_{\mathrm{eff}}}{\partial \lambda}, \tag{6}$$

with λ being the wavelength. The mode index was obtained from the multilayer-waveguide model, where the absorption in the NPL layer was taken into account as obtained from ellipsometry (see Supporting Information, Section S13).

Modal-Gain Calculation. For the modal-gain calculation, the material gain of the gain layer was swept over a range of values. Therefore, the imaginary part of the relative permittivity was set to negative values, while the real part was kept constant. For a given G_{mat}, the corresponding imaginary part of the relative permittivity, $\varepsilon''_{\mathrm{gain}}$, was calculated using[39]

$$\varepsilon''_{\mathrm{gain}} = -\frac{G_{\mathrm{mat}} n_{\mathrm{NPL}}}{k_0}, \tag{7}$$

with n_{NPL} being the real part of the refractive index of the NPL film as measured from ellipsometry (see Supporting Information, Section S13) and $k_0 = 2\pi/\lambda_0$ being the wavevector of the free-space wavelength λ_0.

Laser Rate Equations. To model the power-dependent laser characteristics, we used a coupled rate-equation model[50,51] that describes an excited-carrier population, and two modal populations (surface plasmon and photon) or one modal population (surface plasmon) for laser cavities with a gain-layer thickness above or below the photonic-mode cutoff, respectively (see Supporting Information, Section S15 for details). The carrier population is fed by a time-dependent pump pulse [and reabsorption (corresponding to negative gain)] and decays through spontaneous emission (radiative and non-radiative) and stimulated emission. The surface-plasmon and photon populations grow through spontaneous and stimulated emission and are depleted by Ag and reflection losses (and reabsorption). Note that the Purcell enhancement is being neglected here, as it has been shown that, in cavities of this size, the Purcell effect plays a minor role.[29,52] All model parameters were estimated from experimental data or retrieved from literature reports. The rate equations were solved through numerical integration for a range of pump fluences. The output-photon number was obtained by integrating the mirror loss rate over time.

ASSOCIATED CONTENT

Supporting Information. The Supporting Information is available free of charge on the ACS Publications website at https://pubs.acs.org.

Additional data, supporting calculations, and detailed descriptions of the sample fabrication and optical characterization (PDF)

AUTHOR INFORMATION

Corresponding Author

*Email: dnorris@ethz.ch

ORCID

Marianne Aellen: 0000-0003-1548-0433

Aurelio Rossinelli: 0000-0001-6930-4190

Robert C. Keitel: 0000-0002-9412-8034

Raphael Brechbühler: 0000-0001-7498-9729

Felipe V. Antolinez: 0000-0002-1787-0112

Sergio G. Rodrigo: 0000-0001-6575-168X

Jian Cui: 0000-0002-2394-3357

David J. Norris: 0000-0002-3765-0678

Author Contributions

M.A., J.C., and D.J.N. conceived the ideas and planned the experiments. M.A. designed, fabricated, and optically characterized the laser devices with assistance from R.C.K. and R.B. A.A.R. synthesized the nanoplatelets. M.A. performed the modal-gain and rate-equation calculations with assistance from R.B. and F.V.A. and input from S.G.R. The manuscript was written by M.A., J.C., and D.J.N. with input from all authors. D.J.N. supervised the project.

Funding Sources

This work was supported by the European Research Council under the European Union's Seventh Framework Program (FP/2007–2013) / ERC Grant Agreement Nr. 339905 (QuaDoPS Advanced Grant) and by the Swiss National Science Foundation (SNSF) under grant no. 200021_165559.

Note

The authors declare no competing financial interest.

ACKNOWLEDGMENT

We thank J. Faist and A. Cocina for stimulating discussions and S. Meyer and H. Rojo for technical assistance. We acknowledge the Cleanroom Operations Team of the Binnig and Rohrer Nanotechnology Center (BRNC) for their help and support. Specifically, we would like to acknowledge technical assistance from R. Grundbacher, U. Drechsler, and A. Olziersky. We are grateful to T. Lendenmann, P. Rohner, and D. Poulikakos from the Laboratory of Thermodynamics in Emerging Technologies at ETH Zurich for assistance with and use of their electrohydrodynamic-nanoprinting setup.

REFERENCES

(1) Barnes, W. L.; Dereux, A.; Ebbesen, T. W., Surface Plasmon Subwavelength Optics. *Nature* **2003,** *424*, 824–830.

(2) Maier, S. A., *Plasmonics: Fundamentals and Applications*. Springer: New York, 2007.

(3) Homola, J., Surface Plasmon Resonance Sensors for Detection of Chemical and Biological Species. *Chemical Reviews* **2008,** *108*, 462–493.

(4) Kauranen, M.; Zayats, A. V., Nonlinear Plasmonics. *Nat. Photonics* **2012,** *6*, 737–748.

(5) Oulton, R. F.; Sorger, V. J.; Genov, D. A.; Pile, D. F. P.; Zhang, X., A Hybrid Plasmonic Waveguide for Subwavelength Confinement and Long-Range Propagation. *Nat. Photonics* **2008,** *2*, 496–500.

(6) Min, B.; Ostby, E.; Sorger, V.; Ulin-Avila, E.; Yang, L.; Zhang, X.; Vahala, K., High-Q Surface-Plasmon-Polariton Whispering-Gallery Microcavity. *Nature* **2009,** *457*, 455–458.

(7) Dionne, J. A.; Diest, K.; Sweatlock, L. A.; Atwater, H. A., PlasMOStor: A Metal-Oxide-Si Field Effect Plasmonic Modulator. *Nano Lett.* **2009,** *9*, 897–902.

(8) Melikyan, A.; Alloatti, L.; Muslija, A.; Hillerkuss, D.; Schindler, P. C.; Li, J.; Palmer, R.; Korn, D.; Muehlbrandt, S.; Van Thourhout, D.; Chen, B.; Dinu, R.; Sommer, M.; Koos, C.; Kohl, M.; Freude, W.; Leuthold, J., High-Speed Plasmonic Phase Modulators. *Nat. Photonics* **2014,** *8*, 229–233.

(9) Hill, M. T.; Gather, M. C., Advances in Small Lasers. *Nat. Photonics* **2014,** *8*, 908–918.

(10) Haffner, C.; Heni, W.; Fedoryshyn, Y.; Niegemann, J.; Melikyan, A.; Elder, D. L.; Baeuerle, B.; Salamin, Y.; Josten, A.; Koch, U.; Hoessbacher, C.; Ducry, F.; Juchli, L.; Emboras, A.; Hillerkuss, D.; Kohl, M.; Dalton, L. R.; Hafner, C.; Leuthold, J., All-Plasmonic Mach–Zehnder Modulator Enabling Optical High-Speed Communication at the Microscale. *Nat. Photonics* **2015,** *9*, 525–528.

(11) Emboras, A.; Niegemann, J.; Ma, P.; Haffner, C.; Pedersen, A.; Luisier, M.; Hafner, C.; Schimmel, T.; Leuthold, J., Atomic Scale Plasmonic Switch. *Nano Lett.* **2016,** *16*, 709–714.

(12) Khurgin, J. B., How to Deal with the Loss in Plasmonics and Metamaterials. *Nat. Nanotechnol.* **2015,** *10*, 2–6.

(13) Berini, P.; De Leon, I., Surface Plasmon–Polariton Amplifiers and Lasers. *Nat. Photonics* **2011,** *6*, 16–24.

(14) Bergman, D. J.; Stockman, M. I., Surface Plasmon Amplification by Stimulated Emission of Radiation: Quantum Generation of Coherent Surface Plasmons in Nanosystems. *Phys. Rev. Lett.* **2003,** *90*, 027402.

(15) Azzam, S. I.; Kildishev, A. V.; Ma, R.-M.; Ning, C.-Z.; Oulton, R.; Shalaev, V. M.; Stockman, M. I.; Xu, J.-L.; Zhang, X., Ten Years of Spasers and Plasmonic Nanolasers. *Light Sci. Appl.* **2020,** *9*, 1–21.

(16) Ma, R. M.; Oulton, R. F., Applications of Nanolasers. *Nat. Nanotechnol.* **2019,** *14*, 12–22.

(17) Oulton, R. F.; Sorger, V. J.; Zentgraf, T.; Ma, R. M.; Gladden, C.; Dai, L.; Bartal, G.; Zhang, X., Plasmon Lasers at Deep Subwavelength Scale. *Nature* **2009,** *461*, 629–632.

(18) Wu, C. Y.; Kuo, C. T.; Wang, C. Y.; He, C. L.; Lin, M. H.; Ahn, H.; Gwo, S., Plasmonic Green Nanolaser Based on a Metal-Oxide-Semiconductor Structure. *Nano Lett.* **2011,** *11*, 4256–4260.

(19) Ma, R. M.; Oulton, R. F.; Sorger, V. J.; Bartal, G.; Zhang, X., Room-Temperature Sub-Diffraction-Limited Plasmon Laser by Total Internal Reflection. *Nat. Mater.* **2011,** *10*, 110–113.

(20) Lu, Y. J.; Kim, J.; Chen, H. Y.; Wu, C.; Dabidian, N.; Sanders, C. E.; Wang, C. Y.; Lu, M. Y.; Li, B. H.; Qiu, X.; Chang, W. H.; Chen, L. J.; Shvets, G.; Shih, C. K.; Gwo, S., Plasmonic Nanolaser Using Epitaxially Grown Silver Film. *Science* **2012,** *337*, 450–453.

(21) Zhang, Q.; Li, G.; Liu, X.; Qian, F.; Li, Y.; Sum, T. C.; Lieber, C. M.; Xiong, Q., A Room Temperature Low-Threshold Ultraviolet Plasmonic Nanolaser. *Nat. Commun.* **2014,** *5*, 1–9.

(22) Sidiropoulos, T. P. H.; Roder, R.; Geburt, S.; Hess, O.; Maier, S. A.; Ronning, C.; Oulton, R. F., Ultrafast Plasmonic Nanowire Lasers near the Surface Plasmon Frequency. *Nat. Phys.* **2014,** *10*, 870–876.

(23) Chou, Y. H.; Wu, Y. M.; Hong, K. B.; Chou, B. T.; Shih, J. H.; Chung, Y. C.; Chen, P. Y.; Lin, T. R.; Lin, C. C.; Lin, S. D.; Lu, T. C., High-Operation-Temperature Plasmonic Nanolasers on Single-Crystalline Aluminum. *Nano Lett.* **2016,** *16*, 3179–3186.

(24) Yu, H.; Ren, K.; Wu, Q.; Wang, J.; Lin, J.; Wang, Z.; Xu, J.; Oulton, R. F.; Qu, S.; Jin, P., Organic–Inorganic Perovskite Plasmonic Nanowire Lasers with a Low Threshold and a Good Thermal Stability. *Nanoscale* **2016,** *8*, 19536–19540.

(25) Wu, Z.; Chen, J.; Mi, Y.; Sui, X.; Zhang, S.; Du, W.; Wang, R.; Shi, J.; Wu, X.; Qiu, X.; Qin, Z.; Zhang, Q.; Liu, X., All-Inorganic $CsPbBr_3$ Nanowire Based Plasmonic Lasers. *Adv. Opt. Mater.* **2018,** *6*, 1800674.

(26) Hill, M. T.; Oei, Y.-S.; Smalbrugge, B.; Zhu, Y.; de Vries, T.; van Veldhoven, P. J.; van Otten, F. W. M.; Eijkemans, T. J.; Turkiewicz, J. P.; de Waardt, H.; Geluk, E. J.; Kwon, S.-H.; Lee, Y.-H.; Nötzel, R.; Smit, M. K., Lasing in Metallic-Coated Nanocavities. *Nat. Photonics* **2007,** *1*, 589–594.

(27) Hill, M. T.; Marell, M.; Leong, E. S.; Smalbrugge, B.; Zhu, Y.; Sun, M.; van Veldhoven, P. J.; Geluk, E. J.; Karouta, F.; Oei, Y. S.; Notzel, R.; Ning, C. Z.; Smit, M. K., Lasing in Metal-Insulator-Metal Sub-Wavelength Plasmonic Waveguides. *Opt. Express* **2009,** *17*, 11107–11112.

(28) Ding, K.; Liu, Z.; Yin, L.; Wang, H.; Liu, R.; Hill, M. T.; Marell, M. J. H.; van Veldhoven, P. J.; Nötzel, R.; Ning, C. Z., Electrical Injection, Continuous Wave Operation of Subwavelength-Metallic-Cavity Lasers at 260 K. *Appl. Phys. Lett.* **2011,** *98*, 231108.

(29) Kress, S. J. P.; Cui, J.; Rohner, P.; Kim, D. K.; Antolinez, F. V.; Zaininger, K. A.; Jayanti, S. V.; Richner, P.; McPeak, K. M.; Poulikakos, D.; Norris, D. J., A Customizable Class of Colloidal-Quantum-Dot Spasers and Plasmonic Amplifiers. *Sci. Adv.* **2017,** *3*, e1700688.

(30) Zhu, W.; Xu, T.; Wang, H.; Zhang, C.; Deotare, P. B.; Agrawal, A.; Lezec, H. J., Surface Plasmon Polariton Laser Based on a Metallic Trench Fabry-Perot Resonator. *Sci. Adv.* **2017,** *3*, e1700909.

(31) Wang, S.; Chen, H. Z.; Ma, R. M., High Performance Plasmonic Nanolasers with External Quantum Efficiency Exceeding 10%. *Nano Lett.* **2018,** *18*, 7942–7948.

(32) Wang, S.; Wang, X. Y.; Li, B.; Chen, H. Z.; Wang, Y. L.; Dai, L.; Oulton, R. F.; Ma, R. M., Unusual Scaling Laws for Plasmonic Nanolasers Beyond the Diffraction Limit. *Nat. Commun.* **2017,** *8*, 1889.

(33) Nagpal, P.; Lindquist, N. C.; Oh, S. H.; Norris, D. J., Ultrasmooth Patterned Metals for Plasmonics and Metamaterials. *Science* **2009,** *325*, 594–597.

(34) McPeak, K. M.; Jayanti, S. V.; Kress, S. J.; Meyer, S.; Iotti, S.; Rossinelli, A.; Norris, D. J., Plasmonic Films Can Easily Be Better: Rules and Recipes. *ACS Photonics* **2015,** *2*, 326–333.

(35) Brucoli, G.; Martín-Moreno, L., Effect of Defect Depth on Surface Plasmon Scattering by Subwavelength Surface Defects. *Phys. Rev. B* **2011,** *83*, 075433.

(36) Kress, S. J.; Antolinez, F. V.; Richner, P.; Jayanti, S. V.; Kim, D. K.; Prins, F.; Riedinger, A.; Fischer, M. P.; Meyer, S.; McPeak, K. M.; Poulikakos, D.; Norris, D. J., Wedge Waveguides and Resonators for Quantum Plasmonics. *Nano Lett.* **2015,** *15*, 6267–6275.

(37) Rossinelli, A. A.; Rojo, H.; Mule, A. S.; Aellen, M.; Cocina, A.; De Leo, E.; Schäublin, R.; Norris, D. J., Compositional Grading for Efficient and Narrowband Emission in CdSe-Based Core/Shell Nanoplatelets. *Chem. Mater.* **2019,** *31*, 9567–9578.

(38) Kress, S. J.; Richner, P.; Jayanti, S. V.; Galliker, P.; Kim, D. K.; Poulikakos, D.; Norris, D. J., Near-Field Light Design with Colloidal Quantum Dots for Photonics and Plasmonics. *Nano Lett.* **2014,** *14*, 5827–5833.

(39) Ning, C. Z., Semiconductor Nanolasers. *Phys. Status Solidi B* **2010,** *247*, 774–788.

(40) Guzelturk, B.; Pelton, M.; Olutas, M.; Demir, H. V., Giant Modal Gain Coefficients in Colloidal II–VI Nanoplatelets. *Nano Lett.* **2019,** *19*, 277–282.

(41) Tomar, R.; Kulkarni, A.; Chen, K.; Singh, S.; van Thourhout, D.; Hodgkiss, J. M.; Siebbeles, L. D. A.; Hens, Z.; Geiregat, P., Charge Carrier Cooling Bottleneck Opens up Nonexcitonic Gain Mechanisms in Colloidal CdSe Quantum Wells. *J. Phys. Chem. C* **2019,** *123*, 9640–9650.

(42) Ding, K.; Liu, Z. C.; Yin, L. J.; Hill, M. T.; Marell, M. J. H.; van Veldhoven, P. J.; Nöetzel, R.; Ning, C. Z., Room-Temperature Continuous Wave Lasing in Deep-Subwavelength Metallic Cavities under Electrical Injection. *Phys. Rev. B* **2012,** *85*, 041301.

(43) Ding, K.; Hill, M. T.; Liu, Z. C.; Yin, L. J.; van Veldhoven, P. J.; Ning, C. Z., Record Performance of Electrical Injection Sub-Wavelength Metallic-Cavity Semiconductor Lasers at Room Temperature. *Opt. Express* **2013,** *21*, 4728–4733.

(44) Tiwari, P.; Wen, P.; Caimi, D.; Mauthe, S.; Triviño, N. V.; Sousa, M.; Moselund, K. E., Scaling of Metal-Clad InP Nanodisk Lasers: Optical Performance and Thermal Effects. *Opt. Express* **2021,** *29*, 3915–3927.

(45) Li, G.; Palomba, S.; de Sterke, C. M., A Theory of Waveguide Design for Plasmonic Nanolasers. *Nanoscale* **2018,** *10*, 21434–21440.

(46) Anger, P.; Bharadwaj, P.; Novotny, L., Enhancement and Quenching of Single-Molecule Fluorescence. *Phys. Rev. Lett.* **2006,** *96*, 113002.

(47) Khajavikhan, M.; Simic, A.; Katz, M.; Lee, J. H.; Slutsky, B.; Mizrahi, A.; Lomakin, V.; Fainman, Y., Thresholdless Nanoscale Coaxial Lasers. *Nature* **2012,** *482*, 204–207.

(48) Galliker, P.; Schneider, J.; Eghlidi, H.; Kress, S.; Sandoghdar, V.; Poulikakos, D., Direct Printing of Nanostructures by Electrostatic Autofocussing of Ink Nanodroplets. *Nat. Commun.* **2012,** *3*, 1–9.

(49) Verhagen, E. Subwavelength Light Confinement with Surface Plasmon Polaritons. PhD Thesis, Utrecht Univ., Utrecht, Netherlands, 2009.

(50) Coldren, L. A.; Corzine, S. W.; Mashanovitch, M., *Diode Lasers and Photonic Integrated Circuits*. Wiley: Hoboken, N.J., 2012.

(51) Saxena, D.; Mokkapati, S.; Parkinson, P.; Jiang, N.; Gao, Q.; Tan, H. H.; Jagadish, C., Optically Pumped Room-Temperature GaAs Nanowire Lasers. *Nat. Photonics* **2013,** *7*, 963–968.

(52) Khurgin, J. B.; Noginov, M. A., How Do the Purcell Factor, the Q-factor, and the Beta Factor Affect the Laser Threshold? *Laser Photonics Rev.* **2021**, 2000250.

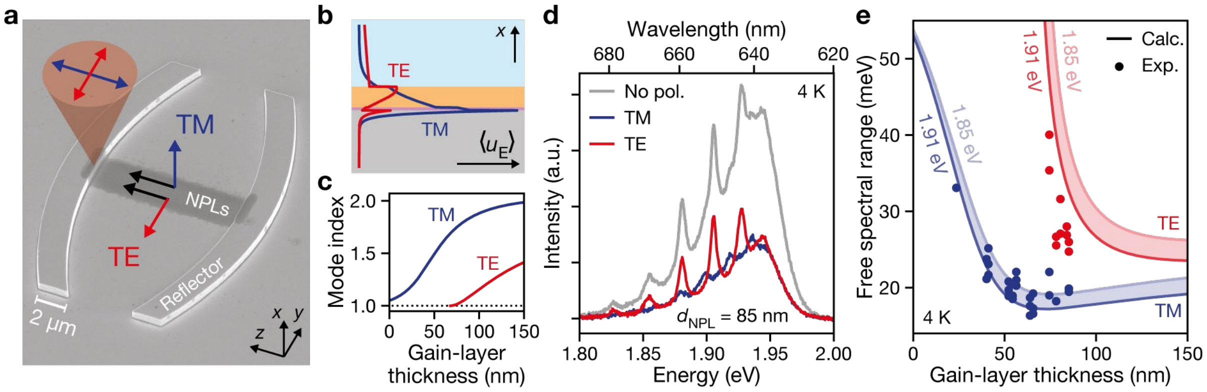

Figure 1. Laser device and waveguide model. (a) Scanning-electron-microscope image of a laser device (tilted view). The Ag reflectors protrude from a smooth, flat Ag surface. A stripe of NPLs is printed into the center of the cavity. Plasmonic and photonic cavity modes with transverse-magnetic (TM, blue) and transverse-electric (TE, red) field components can be distinguished through the polarization of the leakage radiation that is out-scattered at the inner edge of the reflector, as shown. The black arrows denote the propagation direction. The coordinate system indicates the surface normal of the planar multilayer-waveguide model (x) and the two in-plane directions (y and z) from which z is chosen as propagation direction. (b) Calculated mode profiles along the surface normal (x) of the TM (plasmonic, blue) and TE (photonic, red) modes in a planar multilayer-waveguide structure at a free-space wavelength of λ_0 = 635 nm. The mode profiles are plotted as the time-averaged electric energy density, $\langle u_E \rangle$. For each mode, $\langle u_E \rangle$ is normalized by the total energy, U_{EM}, in the mode. The layers are: Ag (grey), 10-nm-thick alumina (purple), 74-nm-thick gain layer (orange), and air (light blue). (c) Effective mode indices of the TM (plasmonic, blue) and TE (photonic, red) modes as a function of gain-layer thickness calculated for a free-space wavelength λ_0 = 635 nm. The photonic mode ceases to exist below ~70 nm. (d) Polarization-resolved cavity spectra within the spontaneous-emission bandwidth of the NPLs excited by a 385-nm LED at 4 K. The unpolarized emission (grey) is composed of cavity modes originating from plasmonic (TM, blue) and photonic (TE, red) propagating modes that are resolved by analyzing the orthogonal polarizations individually. (e) Comparison of the calculated (shaded areas between lines) and experimentally measured (filled circles) free spectral ranges (FSRs) for 1.85–1.91 eV for the plasmonic (blue) and photonic (red) modes. The experimental data points represent various cavities probed at 4 K under LED illumination.

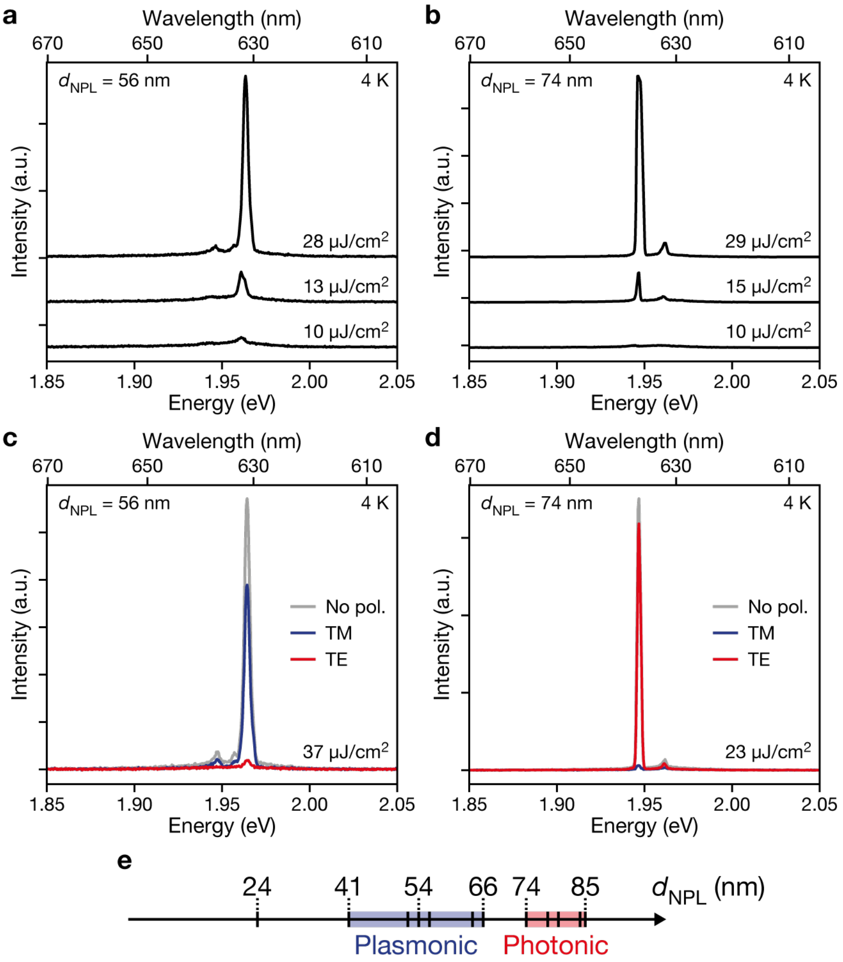

Figure 2. Lasing behavior as a function of NPL-stripe thickness. (a, b) Laser device emission spectra as a function of pump fluence for two devices with NPL-stripe thicknesses, d_{NPL}, of 56 and 74 nm, respectively. The devices were excited at 4 K using a pulsed laser excitation at 405 nm. (c, d) Polarization-resolved lasing spectra reveal the plasmonic (TM, blue) and photonic (TE, red) nature of the lasing emission from (a) and (b), respectively. (e) Twelve probed devices are marked as tick marks on the axis denoting their NPL-stripe thickness. The colored shading indicates which type of mode, plasmonic (blue) or photonic (red), lased in each device. The tick mark at 24 nm, outside of any colored shading, represents a device for which lasing could not be observed.

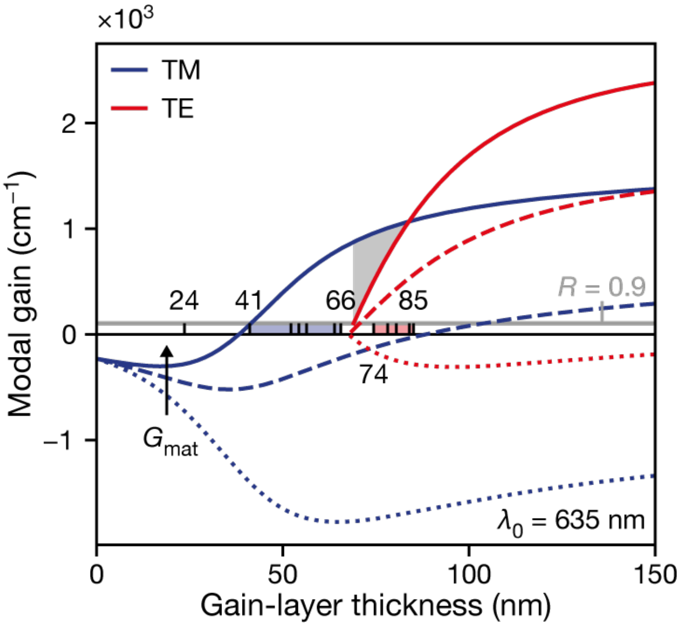

Figure 3. Modal gain as a function of gain-layer thickness. The modal gain for the plasmonic (TM, blue lines) and photonic (TE, red lines) modes at a free-space wavelength λ_0 = 635 nm is plotted as a function of gain-layer thickness for various material-gain values. The calculations are based on the multilayer-waveguide model. The lines represent material-gain values, G_{mat}, of 0 cm^{-1} [corresponding to a transparent gain layer (dotted lines)], 1500 cm^{-1} (dashed lines), and 2500 cm^{-1} (solid lines). The grey horizontal line indicates the reflection losses for a 10-μm-long cavity with mirror reflectivity $R = 0.9$. The grey shaded area marks a regime where the plasmonic modal gain is larger than the photonic modal gain for $G_{\mathrm{mat}} = 2500$ cm^{-1}. The horizontally distributed tick marks indicate experimentally measured devices (the same as in Figure 2e) with colored shading marking which type of mode, plasmonic (blue) or photonic (red), lased in each device. For the device at 24 nm, lasing could not be observed.

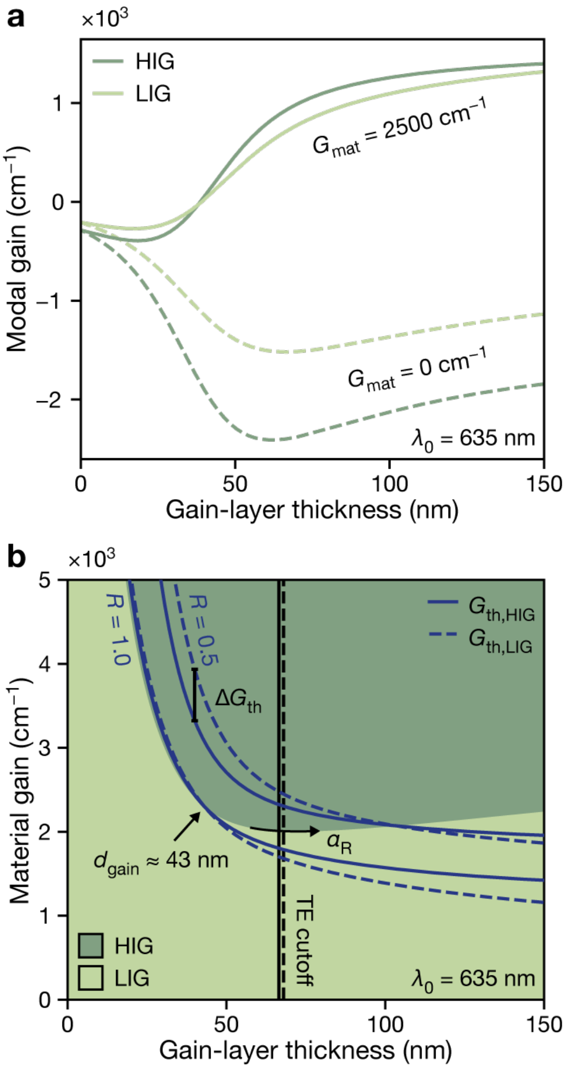

Figure 4. Influence of the gap-layer refractive index on the modal gain. (a) The modal gain of the plasmonic mode plotted as a function of gain-layer thickness for a device with a NPL gain layer and a 10-nm-thick high-index (HIG; $n = 2.13$; dark green) or low-index (LIG; $n = 1.42$; light green) gap layer at a free-space wavelength $\lambda_0 = 635$ nm. The modal gain is plotted for $G_{\mathrm{mat}} = 0\ \mathrm{cm}^{-1}$ (dashed lines) and $G_{\mathrm{mat}} = 2500\ \mathrm{cm}^{-1}$ (solid lines). The structure that experiences a larger modal gain depends on the actual material-gain value. (b) Material gain at which the modal gain is larger for the HIG (dark-green area) or LIG (light-green area) structures for the plasmonic mode. The threshold gains, G_{th}, for the plasmonic modes of the HIG and LIG structures are plotted as solid and dashed blue lines, respectively. They are calculated for a 10-μm-long cavity with mirror reflectivities $R = 1.0$ and 0.5. The arrow at $d_{\mathrm{gain}} \approx 43$ nm indicates the crossing point of the threshold gains for $R = 1.0$. For increasing reflection losses, α_{R}, the threshold-gain crossing moves along the mode-condition border in the direction of the arrow. The difference in threshold gain, ΔG_{th}, for $R = 0.5$ and $d_{\mathrm{gain}} = 40$ nm is 18.4% (vertical bar with caps). The black vertical solid and dashed lines indicate the photonic-mode (TE) cutoff thickness for the HIG and LIG structures, respectively.

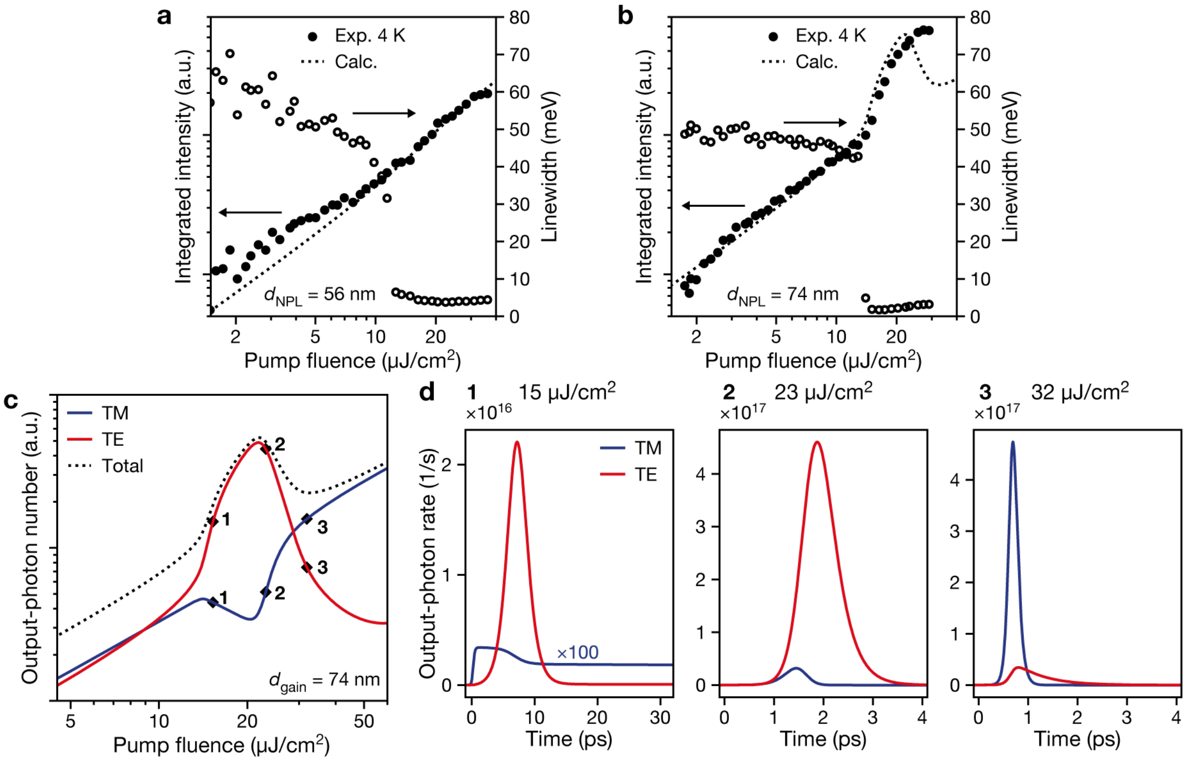

Figure 5. Light–light curves and mode switching. (a, b) Spectrally integrated output intensity (filled circles) as a function of pump fluence for a device with d_{NPL} = 56 nm (same device as in Figure 2a,c) and a device with d_{NPL} = 74 nm (same device as in Figure 2b,d) measured at 4 K under pulsed excitation at 405 nm. Calculated output-photon numbers from the rate-equation model (dotted lines) agree well with the experimentally obtained values. The linewidth of the emission spectrum [obtained by fitting a single Gaussian to the laser device emission spectra under pulsed excitation (spectra presented for a few pump fluences in Figure 2a,b)] indicates the transition from a spontaneous-emission-dominated output to an output with a predominant narrow lasing peak (empty circles). (c) Calculated output-photon number of the plasmonic (TM, blue) and photonic (TE, red) modes for a cavity with d_{gain} = 74 nm. The dotted line indicates the sum of the two. (d) Time evolution of the output-photon rate for the plasmonic (TM, blue) and photonic (TE, red) modes at three different pump fluences, as indicated by the diamonds in (c). The primary lasing mode switches from photonic (diamond 1 and 2) to plasmonic (diamond 3) as the pump fluence increases.

Table of Contents Graphic

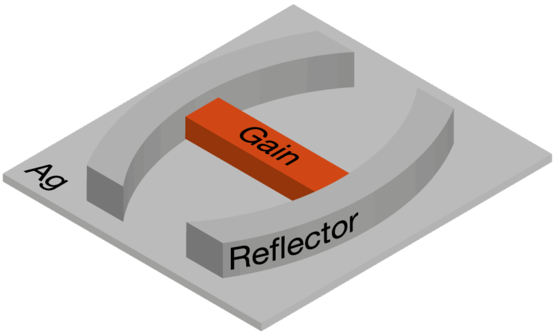
Gain
Ag
Reflector